

A series of climate oscillations around 8.2 ka BP revealed through multi-proxy speleothem records from North China

Pengzhen Duan¹, Hanying Li², Zhibang Ma³, Jingyao Zhao², Xiyu Dong², Ashish Sinha⁴, Peng Hu^{5,6}, Haiwei Zhang², Youfeng Ning², Guangyou Zhu¹, Hai Cheng^{2,7,8}

¹Research Institute of Petroleum Exploration and Development, PetroChina, Beijing, China

²Institute of Global Environmental Change, Xi'an Jiaotong University, Xi'an, China

³Key Laboratory of Cenozoic Geology and Environment, Institute of Geology and Geophysics, Chinese Academy of Sciences, Beijing, China

⁴Department of Earth Science, California State University, Dominguez Hills, Carson, USA

⁵Yunnan Key Laboratory of Meteorological Disasters and Climate Resources in the Greater Mekong Subregion, Yunnan University, Kunming 650091, China

⁶Department of Atmospheric Sciences, Yunnan University, Kunming 650500, China

⁷State Key Laboratory of Loess and Quaternary Geology, Institute of Earth Environment, Chinese Academy of Sciences, Xi'an, China

⁸Key Laboratory of Karst Dynamics, MLR, Institute of Karst Geology, CAGS, Guilin, China

Correspondence to: Hanying Li (hanyingli@xjtu.edu.cn) and Hai Cheng (cheng021@xjtu.edu.cn)

Abstract. The 8.2 ka event has been extensively investigated as a remarkable single event, but rarely considered as a part of multi-centennial climatic evolution. Here, we present absolutely dated speleothem multi-proxy records spanning 9.0–7.9 ka BP from Beijing in North China, near the northern limit of the East Asian summer monsoon (EASM) and thus sensitive to climate change, to provide evidence for the intensified multi-decadal climatic oscillations since **8.52 ka BP**. Three extreme excursions characterized by inter-decadal consecutive $\delta^{18}\text{O}$ excursions exceeding $\pm 1\sigma$ are identified from 8.52 ka BP in our speleothem record. The former two are characterized by enriched ^{18}O at **~8.50** and 8.20 ka BP, respectively, suggesting a prolonged arid event, which is supported by the positive trend in $\delta^{13}\text{C}$ values, increased trace element ratios, and lower growth rate. Following the 8.2 ka event, an excessive rebound immediately emerges in our $\delta^{18}\text{O}$ and trace element records but moderate in the $\delta^{13}\text{C}$, probably suggesting pluvial conditions and nonlinear response of the local ecosystem. Following two similar severe droughts at **8.50** and 8.20 ka BP, the different behavior of $\delta^{13}\text{C}$ suggests the recovering degree of resilient ecosystem responding to different rebounded rainfall intensity. A comparison with other high-resolution records suggests that the two droughts-one pluvial patterns between **8.52** and 8.0 ka BP are of global significance instead of a regional phenomenon, which is causally linked to the slowdown and acceleration of the Atlantic Meridional Overturning Circulation that was further dominated by the freshwater injections in the North Atlantic.

33 **1 Introduction**

34 The overall warming during 9.0–7.9 ka BP (thousand years before present, where the present is 1950 CE) was
35 punctuated by several inter-decadal to centennial climate fluctuations in the Northern Hemisphere (NH). The 8.2 ka
36 event, as the most prominent abrupt cold event registered in the Greenland ice core records within the Holocene
37 (Thomas et al., 2007), has been widely revealed by a large number of marine and terrestrial archives and dated to
38 occur between 8.3–8.0 ka BP with a duration of 150–200 years (Figure S1) (e.g., Alley et al., 1997; Thomas et al.,
39 2007; Kobashi et al., 2007; Cheng et al., 2009; Liu et al., 2013; Morrill et al., 2013; Duan P et al., 2021).

40 With deeper investigation, the “cold event” at 8.2 ka BP is evidenced likely to be a part of larger “set” of cold climate
41 anomalies between 8.6 and 8.0 ka BP (e.g., Rohling and Pälike, 2005). According to marine records, the freshwater
42 drainage(s) of proglacial Lakes Agassiz-Ojibway (LAO) into the North Atlantic, which has commonly been thought
43 to trigger the 8.2 ka event (e.g., Alley et al., 1997; Barber et al., 1999) through weakening the Atlantic meridional
44 overturning circulation (AMOC) and resultant global impact, is supposed to separate into two stages (Ellison et al.,
45 2006; Roy et al., 2011; Godbout et al., 2019, 2020) or multiple outbursts (e.g., Teller et al., 2002; Kleiven et al., 2008;
46 Jennings et al., 2015). The first pulse of freshwater may have induced the freshening of the North Atlantic at 8.55–
47 8.45 ka BP (Lochte et al., 2019), the abrupt sea level jump (Tornqvist and Hijma, 2012; Lawrence et al., 2016), the
48 detrital carbonate peak at ~8.6 ka (Jennings et al., 2015), and deposition of a red-sediment bed in Hudson Strait at
49 ~8.26–8.69 ka BP (Kerwin, 1996; Lajeunesse and St-Onge, 2008). The superimposed effect of two or more successive
50 freshwater drainages, or probably coupled with meltwater flux from the ice sheet (Morrill et al., 2014; Matero et al.,
51 2017), finally led to severe and dramatic cooling events in the NH (Teller et al., 2002; Ellison et al., 2006). This is
52 consistent with the view that the 8.2 ka event commenced at ~8.5 ka BP and persisted until ~8.0 ka BP (Rohling and
53 Pälike, 2005) with more than one multi-decadal or centennial perturbations (e.g., Daley et al., 2009; Domínguez-Villar
54 et al., 2009; Tan et al., 2020; Duan W et al., 2021). However, some terrestrial records, such as the Greenland ice cores
55 (Thomas et al., 2007) and European lake sediments (von Grafenstein et al., 1999; Andersen et al., 2017), only
56 documented a remarkable climate event at ~8.2 ka BP, whereas the counterpart to the preceding perturbation is not
57 registered.

58 On the other hand, the multi-decadal or centennial perturbations aforementioned trended not only to the cold and dry
59 direction in the NH, but also extremely warm and humid condition that has been evidenced in the immediate aftermath
60 of the 8.2 ka event (Andersen et al., 2017; Duan P et al., 2023). In particular, the post-event excessive rebound suggests
61 a major pluvial episode prevailing across a large part of North China (Duan P et al., 2023). However, only one proxy,
62 speleothem $\delta^{18}\text{O}$ (Duan P et al., 2023), is insufficient and thus multi-proxy evidences about the overshoot is necessary,
63 especially from the Asian summer monsoon (ASM) domain where the climate change has a fast atmospheric
64 teleconnection with the high-latitude North Atlantic (Cheng et al., 2020; 2022), to complement our understanding on
65 the dynamics of rapid climatic changes, their underlying mechanisms, and the local ecosystem response.

66 In the context of high-emission greenhouse gas nowadays, the melted Greenland ice sheet will inject huge amount of
67 freshwater into the North Atlantic in the next millennium, which is analogous to the sea level rising scenario during
68 9.0–7.9 ka BP (e.g., Aguiar et al., 2020). Therefore, it is important to elucidate the climate variations in response to
69 the freshwater injections in the past to provide a potential analogy for future behavior, especially in North China where

70 the ecosystem and economic development are highly dependent on hydroclimatic changes. Importantly, our study area
71 is located near the northern fringe of the East Asian summer monsoon (EASM), thus sensitively responding to the
72 variations of EASM intensity (Duan et al., 2014; Li et al., 2017; Ma et al., 2012). Here we provide high temporal
73 resolution speleothem multi-proxy records, including $\delta^{18}\text{O}$, $\delta^{13}\text{C}$, Mg/Ca, Sr/Ca, and Ba/Ca, from Beijing in North
74 China to reconstruct the hydroclimatic variations over the Circum-Bohai Sea Region (CBSR) between 9.0–7.9 ka BP.
75 **Two climate anomalous events occurring before and at 8.2 ka BP, as well as a post-8.2 ka rebound**, are investigated
76 to show the general climate pattern around the abrupt cold event from its triggering, response, and ensuing feedback
77 and further examine the relationship between the ASM and the North Atlantic.

78 **2 Materials and Methods**

79 **2.1 Regional settings and modern climatology**

80 Situated at ~60 km southwest of Beijing in North China, the Huangyuan Cave (39°42' N, 115°54' E, altitude 610 m
81 above sea level) is developed in a Middle Proterozoic dolomite and adjacent to Kulishu (39°41' N, 115°39' E) and
82 Shihua (39°47' N, 115°56' E) Caves (Figure S1). The vegetation above the cave is dominated by secondary-growth
83 deciduous broadleaf trees and shrubs (Ma et al., 2012; Duan et al., 2014). According to the meteorological station's
84 observed data between 1998 and 2010 **CE**, the average annual air temperature and precipitation in the study area are
85 12.2 °C and 540 mm, respectively, with cold dry winters and warm wet summers (Figure 1). The regional precipitation
86 is highly seasonal and mainly concentrates on the summer season **with more than 420 mm occurring from June to**
87 **September**. It has been demonstrated (Duan et al., 2016; Li et al., 2017; Duan P et al., 2023) that the summer
88 precipitation $\delta^{18}\text{O}$ ($\delta^{18}\text{O}_p$) is negatively correlated with the summer rainfall amount over the study area and positively
89 correlated with $\delta^{18}\text{O}_p$ over almost the entire EASM domain, the latter of which is normally **related to** the EASM
90 intensity.

91 Speleothem BH-2, collected from Huangyuan Cave, is ~17 cm in length and ~5 cm in width (Figure 2a). The
92 candlestick shape of speleothem without macroscopic bias of the growth axis signifies that it was deposited under
93 relatively stable conditions (Baker et al., 2007). The $\delta^{18}\text{O}$ results for the section of 15–48 mm from the top of the
94 sample, corresponding to 8.38–8.06 ka BP, have been reported in previous investigation (Duan P et al., 2023). In this
95 study, the multi-proxy results of the entire sample are presented that spans 9.0–7.9 ka BP.

96 **2.2 ^{230}Th dating, stable isotope, and trace element analysis**

97 A total of 22 ^{230}Th dates (Table S1) were performed at University of Minnesota, USA, using Thermo-Finnigan
98 Neptune multi-collector inductively coupled plasma mass spectrometers (MC-ICP-MS, Thermo Scientific). The
99 methods are described in detail in Cheng et al. (2013). We followed standard chemistry procedures to separate uranium
100 and thorium for instrument analysis (Edwards et al., 1987). A triple-spike (^{229}Th - ^{233}U - ^{236}U) isotope dilution method
101 was employed to correct instrumental fractionation and determine U/Th isotopic ratios and concentrations.
102 Uncertainties in U/Th isotopic data were calculated offline at 2σ level. **The chronology for the section of 15 to 48 mm**
103 **is based on the combination of annual banding and ^{230}Th dates as reported in previous study** (Duan P et al., 2023).

104 The stable oxygen and carbon isotopes ($\delta^{18}\text{O}$ and $\delta^{13}\text{C}$) of speleothem BH-2 were determined on a Thermo-Scientific
105 MAT-253 isotope ratio mass spectrometer equipped with an online carbonate device (Kiel IV) at the Institute of
106 Geology and Geophysics, Chinese Academy of Sciences and Isotope Laboratory of Xi'an Jiaotong University. The
107 powdered subsamples weighing $\sim 30\ \mu\text{g}$ were drilled along the central growth axis using a Micromill device and then
108 reacted with $\sim 103\%$ phosphoric acid at $70\ ^\circ\text{C}$. The stable oxygen and carbon isotopic compositions of the generated
109 CO_2 gas were measured with working CO_2 standard gas whose values have been calibrated by two international
110 standards named NBS18 and IAEA-603. All results are reported as the per mil deviation relative to the Vienna Pee
111 Dee Belemnite (VPDB). The reported precision of both $\delta^{18}\text{O}$ and $\delta^{13}\text{C}$ at 1σ level is better than $0.1\ \text{‰}$.

112 Trace element ratios (Mg/Ca, Sr/Ca, Ba/Ca), of which the intensity ratio of emission lines are 285.2 (Mg), 407.8 (Sr),
113 and 493.4 (Ba) nm relative to 373.7 nm (Ca), were measured using Laser Induced Breakdown Spectroscopy (LIBS)
114 following the detailed description in Li et al. (2018). In brief, analyses were performed by pulsing and focusing
115 yttrium-aluminum-garnet-Nd laser beam to 0.1 mm. Emitted plasma from the stalagmite surface was collected by
116 optical fibers and sent to a four-passage spectrometer (Ocean Optics MX500+) to obtain a spectrum within the 200-
117 to 580-nm range. These data were determined through the intensity of characteristic spectral line for each element,
118 and then the intensity ratio of each trace element signal to Ca element was calculated and output as the final result for
119 each point. The obtained record is the median intensity ratio based on 20 pulses at each sampling site after 5 laser
120 shots for pre-cleaning the surface. The measurements were performed continuously along the speleothem's growth
121 axis at 0.3 mm increment and a total of 565 data were obtained. The accuracy of data was ensured through the excellent
122 replicability between two-time measurements instead of inset standard materials because of the overwhelming amount
123 of Ca relative to trace elements in speleothem. The original spectral data were processed using an interface created in
124 MATLAB (2020a). The typical standard deviation for the average intensity ratio is less than 0.02 (without unit).

125 **3 Results**

126 **3.1 ^{230}Th dates and age model**

127 The ^{230}Th dating results of the BH-2 are presented in Table S1, which shows that the BH-2 covers the interval between
128 9.0 and 7.9 ka BP. Almost all dates are in stratigraphic order within uncertainties. The average dating uncertainty is \pm
129 57 years at 2σ level. For the period from 8.25 to 8.11 ka BP, we present the speleothem record from Duan P et al.
130 (2023), which is based on the combination of the annual lamina counting and ^{230}Th dates. In addition, here we use an
131 updated chronology of the BH-2 based on the **Stalage algorithm** (Scholz and Hoffmann, 2011), which includes ten
132 additional ages from the remnant sections (Figure 2b and S2).

133 **3.2 Stable isotopic compositions and growth rate**

134 The BH-2 record contains 663 pairs of $\delta^{18}\text{O}$ and $\delta^{13}\text{C}$ data with a mean temporal resolution of ~ 1.6 years. The $\delta^{18}\text{O}$
135 values range from $-7.1\ \text{‰}$ to $-11.5\ \text{‰}$ with a mean of $-9.3\ \text{‰}$ and $\delta^{13}\text{C}$ values vary from $-8.0\ \text{‰}$ to $-12.1\ \text{‰}$ with an
136 average value of $-10.2\ \text{‰}$ (Figures 2d and 2e). It can be seen that the $\delta^{13}\text{C}$ profile follows the same general patterns as
137 the $\delta^{18}\text{O}$ ($r = 0.63$, $p < 0.01$). Compared to the later stage, although some fluctuations are included, the $\delta^{13}\text{C}$ and $\delta^{18}\text{O}$

138 profiles are relatively invariable before 8.52 ka BP. In contrast, the $\delta^{18}\text{O}$ record exhibits a remarkable positive shift at
139 $\sim 8.52\text{--}8.48$ ka BP, during which period the $\delta^{13}\text{C}$ record shifts less prominently to the positive direction but with a
140 fluctuating increasing trend. The rebound from the positive shift of $\delta^{13}\text{C}$ and $\delta^{18}\text{O}$ profiles is followed by a less variable
141 episode spanning 8.48–8.26 ka BP. Afterward, as the most remarkable feature, both records show extremely positive
142 excursions spanning $\sim 8.26\text{--}8.14$ ka BP (Figure 2). The positive anomaly is followed by a shift to the opposite extreme
143 to reach the most negative stage in the $\delta^{18}\text{O}$ record during 8.14–8.05 ka BP, which is not conspicuous in the $\delta^{13}\text{C}$
144 record.

145 The growth rate of the BH-2 established based on the reconstructed chronology (Figures 2c and S2) is highly variable
146 with two peaks of more than 0.8 mm/year at 8.85 and 8.51 ka BP. It is apparent that speleothem BH-2 was contiguously
147 deposited without visible growth hiatus and the growth rate during 8.51–8.16 ka BP (< 0.15 mm/year) is apparently
148 lower relative to other intervals (> 0.15 mm/year on average). Specifically, there are obvious transitions from higher
149 to lower growth rates at ~ 8.51 ka BP and in the opposite trend at ~ 8.16 ka BP.

150 3.3 Trace element ratios

151 The trace element ratio records of two-time measurements are replicable, suggesting the robustness of LIBS technique
152 (Figure S3). As can be seen, the signals in the records are quite variable (Figures 2 and S3). The correlation coefficients
153 (r) for pairs of Mg/Ca and Sr/Ca, Mg/Ca and Ba/Ca, and Sr/Ca and Ba/Ca, are 0.24 ($p < 0.01$), 0.49 ($p < 0.01$), and 0.47
154 ($p < 0.01$), respectively. Similar to $\delta^{18}\text{O}$ and $\delta^{13}\text{C}$ records, all of the Mg/Ca, Sr/Ca, and Ba/Ca records display positive
155 excursions at ~ 8.50 and 8.20 ka BP despite the relative ambiguity of the former one in the Sr/Ca and the latter one in
156 the Ba/Ca, respectively. Besides, there is another more positive excursion at $\sim 8.88\text{--}8.82$ ka BP in the Ba/Ca ratio
157 record, which is absent in the other two records. After principal component analysis of the three records, the excursions
158 at ~ 8.50 and 8.20 ka BP are especially conspicuous (Figure 2f). Different from the $\delta^{18}\text{O}$ and $\delta^{13}\text{C}$ variability, the PC1
159 result of trace element ratio fluctuates frequently with considerable magnitude and show a general decreasing trend
160 before 8.52 ka BP. In the duration of 8.52–8.48 ka BP, it exhibits a fluctuating positive trend and a rapid rebound.
161 Afterwards, the values remain relatively stable until ~ 8.23 ka BP when another positive excursion commences. In this
162 excursion, the PC1 values culminate at ~ 8.12 ka BP followed by a rapid rebound which indicates the termination of
163 this excursion. The values remain relatively stable after 8.10 ka BP.

164 4 Discussion

165 4.1 Proxy interpretations

166 The replication test of $\delta^{18}\text{O}$ records between the BH-2 from Huangyuan Cave and the KLS12 from nearby Kulishu
167 Cave (Duan W et al., 2021) by using the ISCAM (Intra-site Correlation Age Modeling) algorithm (Fohlmeister, 2012)
168 show significantly positive correlation ($r = 0.62$, $p < 0.05$) during 9.0–7.9 ka BP (Figure S4), strongly suggesting that
169 the influence of kinetic fractionation is likely insignificant and the carbonate deposition process is close to equilibrium
170 (Dorale and Liu, 2009). Hence, the BH-2 $\delta^{18}\text{O}$ signals reflect the changes in drip water $\delta^{18}\text{O}$ which in turn inherit from
171 $\delta^{18}\text{O}_p$ related to the regional hydroclimate variations in general. Notably, the study site is located along the summer

172 monsoon fringe with relatively low annual precipitation, and thus the thermodynamics variations in EASM in the
173 areas can significantly bias the mean annual $\delta^{18}\text{O}$ value, e.g., the summer rainfall amount. Indeed, the modern
174 observations (Duan et al., 2016) and reanalysis results (Cheng et al., 2019; Zhang et al., 2019; He et al., 2021; Duan P
175 et al., 2023; Zhao et al., 2023) have proved that speleothem $\delta^{18}\text{O}$ in the study area can be used as a reliable proxy to
176 indicate the regional precipitation variations and the dynamic changes of the summer monsoon circulation, that is,
177 depleted ^{18}O corresponds to increased rainfall over the study area and strengthened EASM, and vice versa.

178 Under the equilibrium fractionation conditions, the carbon isotope ratios ($\delta^{13}\text{C}$) of speleothem carbonate reflect a
179 mixture of three carbon sources: plant root-respired CO_2 in the soil zone, atmospheric CO_2 , and dissolution of bedrock
180 carbonate (McDermott, 2004), in which the plant-related CO_2 is the most important for the variability of the
181 speleothem $\delta^{13}\text{C}$ (Fairchild et al., 2006; Li Y et al., 2020). It has been suggested that changes in the density of
182 vegetative cover and biomass activity exert a critical impact on the speleothem $\delta^{13}\text{C}$ variations in the study region,
183 instead of the relative ratio of C3 (woody taxa) and C4 (grasses) plants (Duan et al., 2014). This is consistent with our
184 observation that the $\delta^{13}\text{C}$ values of speleothem BH-2 fall between -8 and -12 ‰, which is within the typical range for
185 the C3-dominant plant coverage (McDermott, 2004; Fairchild et al., 2006). Although climate-induced changes in the
186 karst system, like pCO_2 degassing, water infiltration, and prior calcite precipitation (PCP) could also contribute to the
187 $\delta^{13}\text{C}$ changes (Fairchild and Treble, 2009; Li et al., 2020), the significant covariance of $\delta^{13}\text{C}$ and $\delta^{18}\text{O}$ in the BH-2 and
188 minor effect of kinetic fractionations as aforementioned, as well as the unbiased $\delta^{18}\text{O}$ signal inherited from
189 precipitation strongly suggest that the density of vegetative cover, the biomass activity, and the vadose of seepage
190 solution dominated by regional hydroclimatic conditions could play a crucial role in the decadal to centennial scale
191 variations of $\delta^{13}\text{C}$ in speleothem BH-2. **In addition to rainfall amount, the impact of temperature variations are non-**
192 **negligible for the growth of plant and biomass activity as well.**

193 The influence of PCP can be inferred from trace element concentrations such that strong (weak) PCP normally induces
194 a high (low) trace element content relative to the calcium in the speleothem calcite (Johnson et al., 2006; Fairchild
195 and Treble, 2009). In general, higher trace element ratio values indicate overall drier conditions when reduced
196 infiltration and increased residence time in the epikarst above the cave favors faster CO_2 degassing and PCP, inducing
197 relatively higher trace element content in the cave drip-water due to the preferential loss of Ca^{2+} along the deposition
198 path; the opposite processes occur in wetter conditions (e.g., Cruz et al., 2007; Griffiths et al., 2010; Zhang et al.,
199 2018). On the other hand, water-rock interaction may have been enhanced in the aquifer during drier conditions
200 because of the prolonged residence time of fluid in the path way, which tends to favor the leaching of Mg and Sr
201 element from the dolomite host rock (Fairchild et al., 2000) and eventually leads the two elements to enrichment in
202 dripwater, and hence speleothem. Apparently, both above two mechanisms indicate the trace element ratios can be
203 used as a reliable proxy of local wetness conditions. Regarding the speleothem growth rate, the sharp drops and
204 persistent lower values in this proxy corresponding to major positive $\delta^{18}\text{O}$ and $\delta^{13}\text{C}$ excursions signify that it most
205 likely was controlled by a sufficient or insufficient supply of drip water, and hence the local rainfall amount (e.g.,
206 Polyak et al., 2004; Banner et al., 2007).

207 **The discrepancy among proxies could suggest that different factors exert influence on these signals in the meteoric**
208 **water-cave aquifer-drip water-carbonate precipitation processes. One thing should be emphasized here is that although**

209 speleothem both $\delta^{18}\text{O}$ and trace element PC1 in this study is interpreted to reflect local rainfall amount, it doesn't
210 mean that these two parameters are linearly related. In other words, strict correlation between two proxies cannot be
211 always expected. In addition, the $\delta^{18}\text{O}$ from original precipitation can be elevated in the processes from the earth
212 surface to seepage due to possible evaporation loss, broadly resemble the impact of PCP on trace element ratios. Due
213 to the resilience of ecosystem in some degree, plant cover and biomass activity could exhibit more stable patterns
214 relative to the $\delta^{18}\text{O}$ and PC1 proxies and thus delayed or muted signals. Therefore, in this study, proxies are interpreted
215 as followings: the speleothem $\delta^{18}\text{O}$ variations mainly reflect the change of large scale atmospheric circulation and are
216 consistent over the entire EASM region in pattern; trace element ratios mainly come from the change of precipitation
217 amount which further is related to, instead of strictly follow, the atmospheric circulation pattern; the speleothem $\delta^{13}\text{C}$
218 values record the fluctuation of vegetation cover and biomass activity dominated by hydroclimatic conditions. In
219 summary, the broad similarity of multi-proxies ($\delta^{18}\text{O}$, $\delta^{13}\text{C}$, trace element ratios, and growth rate) in speleothem BH-
220 2 lends robust support to that all of them record changes in hydroclimatic characteristics (Fairchild and Treble, 2009),
221 that is, the intensity of the EASM and associated rainfall amount presumably dominating the hydroclimatic
222 variabilities over and in the cave in the study area.

223 4.2 Climate fluctuations between 9.0 and 7.9 ka BP in Beijing

224 The variability of the BH-2 $\delta^{18}\text{O}$ record reveals inter-decadal to multi-decadal dry ($> +1\sigma$) or pluvial ($< -1\sigma$)
225 oscillations from 9.0 to 7.9 ka BP without a distinct long-term trend (Figure 2). One noticeable feature of our $\delta^{18}\text{O}$
226 record is a switch from relatively muted to highly variable episodes divided at ~ 8.52 ka BP, consistent with the absence
227 and dominance of centennial to inter-decadal periodicity before and after 8.52 ka BP, respectively (Figure 2g). The
228 mechanism responsible for this phenomenon could be that, in the background of overall strengthened ASM during
229 9.0-8.0 ka BP, a series of abnormal climate events originating from the northern high latitudes lead to relatively more
230 frequent high-amplitude oscillations in $\delta^{18}\text{O}$ profiles and hence more prominent periodicity.

231 The first persistent drought, indicated by positive $\delta^{18}\text{O}$ excursion exceeding $+1\sigma$ values for more than 15 years, initially
232 started at 8.52 ka BP and terminated at 8.48 ka BP (8.5 ka event herein). The entire event is characterized by a saw-
233 tooth structure with a dramatic 2.5 ‰ increase within ~ 20 years and a 2.2 ‰ rebound within 20 years, indicating a
234 fast weakened EASM, and thus reduced precipitation in the study area. This arid condition is supported by the
235 contemporaneous trace element records which show a remarkable positive shift that seems strictly resemble the $\delta^{18}\text{O}$
236 record regarding both the shape and duration, pointing to the changed dynamic process in the cave in response to the
237 decreased precipitation water supply. Additionally, the high-to-low transition of growth rate commencing ~ 8.52 ka
238 BP presumably results from less drip water supply and further in turn reduced precipitation over the cave, marking
239 the start of the EASM weakening. However, the change of vegetation indicated by the $\delta^{13}\text{C}$ proxy is not immediate.
240 It seems that the increasing $\delta^{13}\text{C}$ trend begins later than other proxies and only exhibits a short excursion, probably
241 indicating the nonlinear response of vegetation evolution to the hydroclimate change, especially in a short-time climate
242 event. This could be related to the delayed shortage of subground water for plant growth and a muted response of
243 ecological processes to the hydroclimatic variability in a relatively wet context as indicated by low $\delta^{18}\text{O}$ and trace
244 element values surrounding this excursion (Duan P et al., 2021).

245 Following the end of above arid excursion, another centennial oscillation in much temperate mode persisted to ~8.25
246 ka BP. Subsequently, the BH-2 $\delta^{18}\text{O}$ exhibited the most remarkable droughts with centennial positive excursion
247 between ~8.26 and 8.11 ka BP, conservatively corresponding to the 8.2 ka event (Duan P et al., 2023). This drought
248 event is also proved in the trace element records via the increased values, in concert with the decreased seepage water
249 and hence enhanced PCP. In detailed structure, these trace element ratio records commonly show prominent positive
250 excursion at ~8.20 and 8.14 ka BP, the latter of which is especially elevated in them. However, the slowly increased
251 pattern in the trace element ratio records from 8.26 to 8.18 ka BP is quite distinct from the $\delta^{18}\text{O}$ record in which its
252 values dramatically increase in the first 70 years, suggesting the probably nonlinear relationship between regional
253 climate ($\delta^{18}\text{O}$) and local hydroclimatic condition (trace element ratios). Moreover, in this event, the $\delta^{13}\text{C}$ exhibits a
254 prominent positive shift, pointing to the decay of the ecosystem in this severe drought event. It is noteworthy that the
255 variation pattern of $\delta^{13}\text{C}$ in the 8.2 ka event is more similar to the $\delta^{18}\text{O}$ relative to **the 8.5 ka event**. This absence of
256 muted $\delta^{13}\text{C}$ signal suggests the close relationship between the vegetation and regional hydroclimatic conditions in a
257 long duration and more severe climatic deterioration. Intriguingly, the lower excursion of growth rate somehow
258 predates other proxies. This inter-proxy discrepancy suggests that there are other potential factors, such as the
259 temperature (Wong et al., 2015), controlling the cave dynamic processes, and the growth rate could be a more
260 qualitative indicator to broadly constrain the hydroclimatic conditions in combination with other proxies.

261 Afterward, the hydroclimatic conditions go to the reverse side of the extreme, manifesting a multi-decadal excessive
262 rebound (i.e., overshoot) attaining the lowest $\delta^{18}\text{O}$ values (-11.5 ‰) of the entire record, suggesting the strongest
263 pluvial event (Duan P et al., 2023). This overshoot is additionally supported by trace element ratio record which show
264 quite low values relative to the period before **8.52 ka BP**. However, the rebound of the $\delta^{13}\text{C}$ during the post-8.2 ka
265 event is not as conspicuous as the $\delta^{18}\text{O}$ overshoot and only reaches the mean level of that preceding **the 8.5 ka event**.

266 These features further illustrate the aforementioned nonlinear relationship among the variabilities of regional climate,
267 local hydrological condition, and ecosystem. In other words, the coverage of vegetation and soil microbiological
268 activity during the overshoot event didn't recover to the initial conditions before the 8.2 ka event.

269 The different behavior of $\delta^{13}\text{C}$ after two similar severe droughts at **8.50** and 8.20 ka BP suggests the degree of resilient
270 ecosystem to the different rebound rainfall intensity. For **the 8.5 ka event**, the subsequent rebound of $\delta^{13}\text{C}$ to its prior
271 value suggests the high-level resilience of the plant community to environmental variations under the moderate
272 precipitation amount as indicated by the $\delta^{18}\text{O}$ and trace element ratio records. In contrast, the suddenly excessive
273 increase of precipitation after the 8.2 ka event, which was much more than that before the event, could have suppressed
274 the recovery of vegetation and soil biological activity and thus the moderate rebound of $\delta^{13}\text{C}$ values. Theoretically,
275 the longer weakened atmospheric circulation during the 8.2 ka event and reduced precipitation presumably induced
276 deteriorated vegetation as well as poor-developed soil. However, it seems that the precipitation intensity after the 8.2
277 ka event exerted a key role on the recovery of vegetation density and soil productivity. Specifically, the severe 8.2 ka
278 drought event had a profoundly negative impact on the vegetation-soil system and led them to become more vulnerable
279 under the water shortage conditions. On the other hand, the excessive precipitation after this drought could cause soil
280 erosion and further ecological damage, suppressing the ecosystem recovery above the cave as well as the $\delta^{13}\text{C}$ signals

281 in speleothem. Conclusively, the ecosystem in this karst region was quite vulnerable and the variability of the
282 vegetation-soil system here was tied to local hydrologic conditions with both high and low thresholds.

283 To summarize, akin to the $\delta^{18}\text{O}$ record, other proxy records of the BH-2 (Figure 2) delineate two major drought events,
284 indicated by prominent excursions centered at 8.50 and 8.20 ka BP, respectively, suggesting vegetation degeneration
285 (Duan et al., 2014) and elevated prior calcite precipitation (PCP) arising from longer residence time of solution in the
286 karst aquifer (e.g., Johnson et al., 2006; Fairchild et al., 2009), both of which responded to the deteriorated
287 hydroclimatic conditions. The discrepancy between them could suggest that other drivers than only hydroclimatic
288 conditions possibly have played a non-negligible role in the processes of speleothem formation. In particular, the
289 intensity of the EASM ($\delta^{18}\text{O}$) and the precipitation amount (trace element ratio) over the study area presumably were
290 definitely correlated on a broad pattern but did not necessarily exactly follow each other.

291 **4.3 Spatial patterns for the two drought-one pluvial pattern and underlying mechanisms**

292 This two drought-one pluvial pattern from 8.52 to 8.0 ka BP in speleothem BH-2 represents global scale climate
293 disturbance signals rather than a regional phenomenon since these climate excursions have been widely documented
294 (Figures 3 and S1). In the ASM domain, speleothem records from such as Lianhua (Dong et al., 2018), Wuya (Tan et
295 al., 2020) Caves in North and Northwest China, and Qingtian Cave (Liu et al., 2015) in central China exhibit consistent
296 structure with the BH-2 at around 8.2 ka BP. In particular, a broad anomaly spanning ~340 years between 8.46 and
297 8.12 ka BP has been revealed (Tan et al., 2020) and we find the post-8.2 ka overshoot is also distinguishable (Figure
298 3) in the speleothem $\delta^{18}\text{O}$ record from the western Chinese Loess Plateau which is situated in the northern limit of the
299 ASM. Unlike these north-located records, although a prominent 8.2 ka event is documented in speleothem of Heshang
300 Cave in central China (Liu et al., 2013), the preceded excursion is ambiguous and the post-8.2 ka event anomaly is
301 absent. Coincidentally, a similar phenomenon seems to occur in the central monsoon domain, like Dongge Cave in
302 South China (Cheng et al., 2009) and Tham Doun Mai Cave from northern Laos (Wood et al., 2023). This probably
303 suggests that, compared to the low latitudes, the climate in the north part (or the margin area) of the ASM is more
304 sensitive to the climate perturbation signals originating from the high northern latitude regions. Through affecting the
305 westerly changes, high northern latitude climate variations can finally strongly influence the EASM (Chiang et al.,
306 2015; Duan et al., 2016; Tan et al., 2020).

307 In the low latitudes of the Indian summer monsoon realm, the speleothem $\delta^{18}\text{O}$ record from Hoti Cave is remarkably
308 consistent with the pattern in our record. Specifically, Hoti Cave record shows positive $\delta^{18}\text{O}$ excursions by ~2 ‰ in
309 amplitude centering ~8.42 ka BP and a growth hiatus at 8.2 ka BP surrounded by enriched ^{18}O , pointing to the drought
310 conditions due to the weakened Indian summer monsoon attendant with a southward shift of the intertropical
311 convergence zone (ITCZ). After the growth resumption, an overshoot can be identified (Cheng et al., 2009). It happens
312 that the two positive excursions are quite pronounced in nearby Qunf Cave (Figure 3) (Cheng et al., 2009), whereas
313 the overshoot is absent. Collectively, records from more sensitive areas in the ASM domain intactly preserved the two
314 drought-one pluvial pattern, while the pre-8.2 ka event or the overshoot is missed in records from insensitive regions.
315 In the North Atlantic region, Greenland ice core $\delta^{18}\text{O}$ (Thomas et al., 2007) and reconstructed temperature based on
316 argon and nitrogen isotopes (Kobashi et al., 2017) captured both the 8.2 ka event and ensuing overshoot, and the pre-

317 8.2 ka event is apparent in the temperature profile but ambiguous or slightly excused (Jennings et al., 2015) in the
318 $\delta^{18}\text{O}$ records. Indeed, the atmospheric circulation over Greenland has substantially changed since ~ 8.5 ka BP as
319 suggested by increased potassium and calcium ions, indicators of dust supply to Greenland, as well as decreased snow-
320 accumulation rate (Rohling and Pälike, 2005; Kobashi et al., 2017; Burstyn et al., 2019). The absent signal of the pre-
321 8.2 ka event in $\delta^{18}\text{O}$ records could be attributed to the compensation of other processes like precipitation seasonality
322 and summer warming (He et al., 2021). The prolonged climate anomalies around 8.2 ka BP are **further supported by**
323 **two negative anomalies in speleothem $\delta^{18}\text{O}$ records from Italy (Domínguez-Villar et al., 2009) and Hungary (Demény**
324 **et al., 2023), lower tree ring width from 8.42 to 8.0 ka BP in Germany (Spurk et al., 2002)**, as well as degraded climate
325 conditions between 8.45 and 8.10 ka BP revealed by speleothem proxies from Père Noël Cave in Belgium (Allan et
326 al., 2017). All of these collectively suggest a series of pronounced climate oscillations between 8.5 and 8.0 ka BP,
327 instead of merely the 8.2 ka event, is of hemispheric significance (Rohling and Pälike, 2005). In the North America,
328 multi-proxy speleothem records manifest more sustained increase in precipitation in both precursor and 8.2 ka event
329 responding to the increased North Pacific storm in California (de Wet et al., 2021).

330 Similar but antiphase patterns are observed in the records from the Southern Hemisphere. For example, it appears that
331 speleothem record from Lapa Grand Cave in East Brazil (Stríkis et al., 2011) captured the two pluvial-one drought
332 structure (Figure 3). **Intriguingly, although speleothem record from Padre Cave (Cheng et al., 2009) fails to preserve**
333 **a remarkable pre-8.2 ka event (Figure 3), two negative short excursions and a seemingly negative trend can be**
334 **observed from 8.34 to 8.23 ka BP.** Besides, the beginning deposit of speleothem in Padre Cave at ~ 8.5 ka BP, coeval
335 with the reduced precipitation in the ASM domain, likely reflects more favorable hydroclimatic conditions due to
336 more precipitation, which in turn could arise from intensified South American summer monsoon associated with the
337 southward displacement of the ITCZ (Wang X et al., 2004), suggesting the possible occurrence of the pre-8.2 ka event
338 there. Coincidentally, the speleothem growth resumption after a long hiatus (Duan P et al., 2021), together with the
339 negative trend of speleothem $\delta^{18}\text{O}$ record (Voarintsoa et al., 2019) in Northwest Madagascar commenced at ~ 8.5 ka
340 BP and persisted until the end of the 8.2 ka event, indicative of more precipitation in response to the southward ITCZ
341 shift, suggesting the extent of the pre-8.2 ka event to the East Africa monsoon domain. However, the post-8.2 ka event
342 was not clearly identified by the Northwest Madagascar record and thus more evidence is needed.

343 The two droughts-one pluvial pattern revealed in our BH-2 records could mainly correspond to the waxing and waning
344 of drainages of the **lakes Agassiz and Ojibway (LAO)** (Barber et al., 1999; Ellison et al., 2006) and contemporary ice
345 sheet melted freshwater flux (Matero et al., 2017, 2020) (Figure 3), both of which causally related to the AMOC
346 strength dynamics. Firstly, the major two-step outburst of the LAO (e.g., Ellison et al., 2006; Kleiven et al., 2008;
347 Jennings et al., 2015; Lochte et al., 2018; Godbout et al., 2019, 2020) and the continuous Laurentide Ice Sheet (LIS)
348 melting together contributed to the increase of total freshwater flux (e.g., Morrill et al., 2014; Matero et al., 2017,
349 2020), inducing observed sea level rise in North Atlantic commencing ~ 8.5 ka BP (Hijma et al., 2010), cooling
350 conditions initially in the circum-North Atlantic region and perturbed into other areas through fast atmospheric
351 propagations (Cheng et al., 2009, 2020; Liu et al., 2013; Buizert et al., 2014; Duan P et al., 2021). Coincident with
352 enriched $^{18}\text{O}_p$ in most ASM domains, the intensity of the East Asian summer monsoon was weakened (Cheng et al.,
353 2009) and less precipitation fell in the Beijing area (Duan P et al., 2023). In contrast, due to the southward displacement

354 of the ITCZ in response to the hemispheric thermal contrast, the Southern Hemisphere, like Northeast Madagascar
355 and East Brazil, received more precipitation (i.e., stronger monsoon) and thus speleothem records there exhibit
356 depleted $^{18}\text{O}_p$. Further, the simulated smaller freshwater flux peak at ~ 8.5 ka BP relative to the second one at 8.2 ka
357 (Figure 3) (Matero et al., 2020) could provide a potential explanation for the lower amplitude and shorter duration of
358 the pre-8.2 ka event relative to the 8.2 ka event in our record and the absence of the pre-8.2 ka event in other records.
359 Additionally, the 8.2 ka event is preceded by a remarkable reduction in solar activity by $\sim 1 \text{ Wm}^{-2}$ with a duration of
360 ~ 150 years, beginning at ~ 8.45 ka BP (Rohling and Pälike, 2005; Steinhilber et al., 2009; Wanner et al., 2011; Burstyn
361 et al., 2019), and an increase in the magnitude and frequency of volcanic eruptions (Kobashi et al., 2017; Burstyn et
362 al., 2019), both of which are also thought to contribute to the prolonged climate disturbance via different impacts on
363 atmospheric processes.

364 On the other hand, the overshoot in the ASM domain could be remotely related to the higher temperature in the North
365 Atlantic (Kobashi et al., 2017; Andersen et al., 2017) (Figure 3) which in turn possibly arose from the remarkably
366 speed-up AMOC (Ellison et al., 2006; Renold et al., 2010; Mjell et al., 2015; Andersen et al., 2017). The accelerated
367 AMOC led to more heat release in the North Atlantic and anomalously strengthened ASM. In the meanwhile, the
368 ITCZ and associated rainbelt were displaced northwards, causing less precipitation in east Brazil as evidenced by
369 positive $\delta^{18}\text{O}$ excursion of speleothem from Lapa Grande Cave (Figure 3).

370 **5 Conclusions**

371 **The multi-proxy records of speleothem BH-2 from Beijing, North China document the multi-decadal to centennial**
372 **scale hydroclimate changes with two arid episodes at ~ 8.5 and 8.2 ka BP**, and an immediately ensuing excessive
373 rebound after the 8.2 ka event. A comparison with other paleoclimate records suggests that these prominent climate
374 fluctuations with two drought-one pluvial pattern should be a global signal instead of a regional phenomenon. We
375 propose that the slowdown and resumption of the AMOC controlled by the freshwater flux into the North Atlantic and
376 the resultant reorganization of the atmospheric circulation during the study stage mainly contribute to the arid and
377 pluvial excursions, and the influence of volcanic outbursts and reduced solar activity are also non-negligible.

378 **Data availability**

379 All data needed to evaluate the conclusions in the paper are presented in the paper. The data will be archived at the
380 NOAA National Climate Data Center (<https://www.ncdc.noaa.gov/data-access/paleoclimatology-data>) when this
381 manuscript is accepted.

382 **Author contributions**

383 PD, HL and HC designed the research and experiments. PD wrote the first draft of the paper. HL, HC, and AS
384 revised the manuscript. ZM did the fieldwork and collected the samples. ZM and HC conducted the ^{230}Th dating.
385 ZM, HC, and PD conducted the oxygen isotope measurements. All authors discussed the results and provided inputs
386 on the manuscript.

387 **Competing interests**

388 The authors declare that they have no conflict of interest.

389 **Acknowledgments**

390 This work was supported by the National Natural Science Foundation of China grants (42150710534 and 41888101
391 to H.C.). We specially thank Ming Tan and Wuhui Duan from Institute of Geology and Geophysics, Chinese Academy
392 of Sciences for their helpful suggestions.

393 **References**

394 Aguiar, W., Meissner, K. J., Montenegro, A., Prado, L., Wainer, I., and Carlson, A. E.: Magnitude of the 8.2 ka event
395 freshwater forcing based on stable isotope modelling and comparison to future Greenland melting, *Sci. Rep.*, 11, 1–
396 10, <https://doi.org/10.1038/s41598-021-84709-5>, 2021.

397 Allan, M., Fagel, N., van der Lubbe, H. J. L., Vonhof, H. B., Cheng, H., Edwards, R. L., and Verheyden, S.: High-
398 resolution reconstruction of 8.2-ka BP event documented in Père Noël cave, southern Belgium, *J. Quat. Sci.*, 33, 840–
399 852, <https://doi.org/10.1002/jqs.3064>, 2018.

400 Alley, R. B., Mayewski, P. A., Sowers, T., Stuiver, M., Taylor, K. C., and Clark, P. U.: Holocene climatic instability:
401 a prominent, widespread event 8200 yr ago, *Geology*, 25, 483–486, [https://doi.org/10.1130/0091-](https://doi.org/10.1130/0091-402)
402 [7613\(1997\)025<0483: HCIAPW>2.3.CO;2](https://doi.org/10.1130/0091-7613(1997)025<0483:HCIAPW>2.3.CO;2), 1997.

403 Andersen, N., Lauterbach, S., Erlenkeuser, H., Danielopol, D. L., Namiotko, T., and Hüls, M.: Evidence for higher-
404 than-average air temperatures after the 8.2 ka event provided by a Central European $\delta^{18}\text{O}$ record, *Quat. Sci. Rev.*, 172,
405 96–108, <http://dx.doi.org/10.1016/j.quascirev.2017.08.001>, 2017.

406 Banner, J. L., Guilfoyle, A., James, E. W., Stern, L. A., and Musgrove, M.: Seasonal variations in modern speleothem
407 calcite growth in central Texas, USA, *J. Sediment. Res.*, 77, 615–622, <https://doi.org/10.2110/jsr.2007.065>, 2007.

408 Barber, D. C., Dyke, A., Hillaire-Marcel, C., Jennings, A. E., Andrews, J. T., and Kerwin, M. W.: Forcing of the cold
409 event of 8,200 years ago by catastrophic drainage of Laurentide lakes, *Nature*, 400, 344, <https://doi.org/10.1038/22504>,
410 1999.

411 Baker, A., Asrat, A., Fairchild, I. J., Leng, M. J., Wynn, P. M., Bryant, C., Genty, D., and Umer, M.: Analysis of the
412 climate signal contained within $\delta^{18}\text{O}$ and growth rate parameters in two Ethiopian stalagmites, *Geochim. Cosmochim.*
413 *Acta.*, 71, 2975–2988, <https://doi.org/10.1016/j.gca.2007.03.029>, 2007.

414 Buizert, C., Sigl, M., Severi, M., Markle, B. R., Wettstein, J. J., and McConnell, J. R.: Abrupt ice-age shifts in southern
415 westerly winds and Antarctic climate forced from the north, *Nature*, 563, 681–685, [https://doi.org/10.1038/s41586-](https://doi.org/10.1038/s41586-416)
416 [018-0727-5](https://doi.org/10.1038/s41586-018-0727-5), 2018.

417 Burstyn, Y., Martrat, B., Lopez, J. F., Iriarte, E., Jacobson, M. J., Lone, M. A., and Deininger, M.: Speleothems from
418 the Middle East: an example of water limited environments in the SISAL database, *Quaternary*, 2, 16,
419 <https://doi.org/10.3390/quat2020016>, 2019.

420 Cheng, H., Edwards, R. L., Shen, C. C., Polyak, V. J., Asmerom, Y., and Woodhead, J.: Improvements in ^{230}Th dating,
421 ^{230}Th and ^{234}U half-life values, and U-Th isotopic measurements by multi-collector inductively coupled plasma mass
422 spectrometry, *Earth. Planet. Sci. Lett.*, 371–372, 82–91, <https://doi.org/10.1016/j.epsl.2013.04.006>, 2013.

423 Cheng, H., Fleitmann, D., Edwards, R. L., Wang, X., Cruz, F. W., and Auler, A. S.: Timing and structure of the 8.2
424 kyr B.P. event inferred from $\delta^{18}\text{O}$ records of stalagmites from China, Oman, and Brazil, *Geology*, 37, 1007–1010,
425 <https://doi.org/10.1130/G30126A.1>, 2009.

426 Cheng, H., Li, H., Sha, L., Sinha, A., Shi, Z., Yin, Q., Lu, Z., Zhao, D., Cai, Y., Hu, Y., Hao, Q., Tian, J., Kathayat,
427 G., Dong, X., Zhao, J., and Zhang, H.: Milankovitch theory and monsoon, *Innovation*, 3, 100338,
428 <https://doi.org/10.1016/j.xinn.2022.100338>, 2022.

429 Cheng, H., Zhang, H., Spotl, C., Baker, J., Sinha, A., and Li, H.: Timing and structure of the Younger Dryas event
430 and its underlying climate dynamics, *Proc. Natl. Acad. Sci. USA.*, 117, 23408–23417,
431 <https://doi.org/10.1073/pnas.2007869117>, 2020.

432 Cheng, H., Zhang, H., Cai, Y., Shi, Z., Yi, L., Deng, C., and Perez-Mejías, C.: Orbital-scale Asian summer monsoon
433 variations: Paradox and exploration, *Sci. China. Earth. Sci.*, 64, 529–544, [https://doi.org/10.1007/s11430-020-9720-](https://doi.org/10.1007/s11430-020-9720-y)
434 [y](https://doi.org/10.1007/s11430-020-9720-y), 2021.

435 Chiang, J. C., Fung, I. Y., Wu, C. H., Cai, Y., Edman, J. P., Liu, Y., and Labrousse, C. A.: Role of seasonal transitions
436 and westerly jets in East Asian paleoclimate. *Quat. Sci. Rev.*, 108, 111–129,
437 <https://doi.org/10.1016/j.quascirev.2014.11.009>, 2015.

438 Cruz, F., Burns, S., Jercinovic, M., Karmann, I., Sharp, W., and Vuille, M.: Evidence of rainfall variations in Southern
439 Brazil from trace element ratios (Mg/Ca and Sr/Ca) in a Late Pleistocene stalagmite, *Geochim. Cosmochim. Acta.*,
440 71, 2250–2263, <https://doi.org/10.1016/j.gca.2007.02.005>, 2007.

441 Daley, T. J., Street-Perrott, F. A., Loader, N. J., Barber, K. E., Hughes, P. D., Fisher, E. H., and Marshall, J. D.:
442 Terrestrial climate signal of the “8200 yr BP cold event” in the Labrador Sea region, *Geology*, 37, 831–834,
443 <https://doi.org/10.1130/G30043A.1>, 2009.

444 Domínguez-Villar, D., Fairchild, I. J., Baker, A., Wang, X., Edwards, R. L., and Cheng, H.: Oxygen isotope
445 precipitation anomaly in the North Atlantic region during the 8.2 ka event, *Geology*, 37, 1095–1098,
446 <https://doi.org/10.1130/G30393A.1>, 2009.

447 Dong, J., Shen, C. C., Kong, X., Wu, C. C., Hu, H. M., Ren, H., and Wang, Y.: Rapid retreat of the East Asian summer
448 monsoon in the middle Holocene and a millennial weak monsoon interval at 9 ka in northern China, *J. Asian. Earth.*
449 *Sci.*, 151, 31–39, <https://doi.org/10.1016/j.jseaes.2017.10.016>, 2018.

450 Dorale, J. A., and Liu, Z.: Limitations of Hendy test criteria in judging the paleoclimatic suitability of speleothems
451 and the need for replication, *J. Caves. Karst. Stud.*, 71, 73–80, 2009.

452 Duan, P., Li, H., Sinha, A., Voarintsoa, N. R. G., Kathayat, G., Hu, P., and Cheng, H.: The timing and structure of the
453 8.2 ka event revealed through high-resolution speleothem records from northwestern Madagascar, *Quat. Sci. Rev.*,
454 268, 107104, <https://doi.org/10.1016/j.quascirev.2021.107104>, 2021.

455 Duan, P., Li, H., Ma, Z., Zhao, J., Dong, X., Sinha, A., and Cheng, H.: Interdecadal to centennial climate variability
456 surrounding the 8.2 ka event in North China revealed through an annually resolved speleothem record from Beijing,
457 *Geophys. Res. Lett.*, 50, e2022GL101182, <https://doi.org/10.1029/2022GL101182>, 2023.

458 Duan, W., Ma, Z., Tan, M., Cheng, H., Edwards, R. L., and Wen, X.: Timing and structure of early-Holocene climate
459 anomalies inferred from north Chinese stalagmite records, *Holocene*, 31, 1777–1785,
460 <https://doi.org/10.1177/09596836211033218>, 2021.

461 Duan, W., Ruan, J., Luo, W., Li, T., Tian, L., and Zeng, G.: The transfer of seasonal isotopic variability between
462 precipitation and drip water at eight caves in the monsoon regions of China, *Geochim. Cosmochim. Acta.*, 183, 250–
463 266, <http://dx.doi.org/10.1016/j.gca.2016.03.037>, 2016.

464 Duan, W., Tan, M., Ma, Z., and Cheng, H.: The palaeoenvironmental significance of $\delta^{13}\text{C}$ of stalagmite BH-1 from
465 Beijing, China during Younger Dryas intervals inferred from the grey level profile, *Boreas*, 43, 243–250,
466 <https://doi.org/10.1111/bor.12034>, 2014.

467 Edwards, R. L., Chen, J. H., and Wasserburg, G. J.: ^{238}U - ^{234}U - ^{230}Th - ^{232}Th systematics and the precise measurement
468 of time over the past 500,000 years, *Earth Planet. Sci. Lett.*, 81, 175–192, <https://doi.org/10.1016/0012->
469 [821X\(87\)90154-3](https://doi.org/10.1016/0012-821X(87)90154-3), 1987.

470 Ellison, C. R., Chapman, M. R., and Hall, I. R.: Surface and deep ocean interactions during the cold climate event
471 8200 years ago, *Science*, 312, 1929–1932, <https://doi.org/10.1126/science.1127213>, 2006.

472 Fairchild, I. J., Borsato, A., Tooth, A. F., Frisia, S., Hawkesworth, C. J., Huang, Y., and Spiro, B.: Controls on trace
473 element (Sr-Mg) compositions of carbonate cave waters: implications for speleothem climatic records, *Chem. Geol.*,
474 166, 255–269, [https://doi.org/10.1016/S0009-2541\(99\)00216-8](https://doi.org/10.1016/S0009-2541(99)00216-8), 2000.

475 Fairchild, I. J., Smith, C. L., Baker, A., Fuller, L., Spötl, C., Matthey, D., *Chem. Geol.*, and McDermott, F.: Modification
476 and preservation of environmental signals in speleothems, *Earth. Sci. Rev.*, 75, 105–153,
477 <https://doi.org/10.1016/j.earscirev.2005.08.003>, 2006.

478 Fairchild, I. J., *Chem. Geol.*, and Treble, P. C.: Trace elements in speleothems as recorders of environmental change,
479 *Quat. Sci. Rev.*, 449–468, <https://doi.org/10.1016/j.quascirev.2008.11.007>, 2009.

480 Fleitmann, D., Burns, S. J., Mudelsee, M., Neff, U., Kramers, J., Mangini, A., and Matter, A.: Holocene forcing of the
481 Indian monsoon recorded in a stalagmite from southern Oman, *Science*, 300, 1737–1739,
482 <https://doi.org/10.1126/science.1083130>, 2003.

483 Fohlmeister, J.: A statistical approach to construct composite climate records of dated archives, *Quat. Geochronol.*,
484 14, 48–56, <https://doi.org/10.1016/j.quageo.2012.06.007>, 2012.

485 Gauthier, M. S., Kelley, S. E., and Hodder, T. J.: Lake Agassiz drainage bracketed Holocene Hudson Bay ice saddle
486 collapse, *Earth Planet. Sci. Lett.*, 544, 116372, <https://doi.org/10.1016/j.epsl.2020.116372>, 2020.

487 Godbout, P. M., Roy, M., and Veillette, J. J.: High-resolution varve sequences record one major late-glacial ice
488 readvance and two drainage events in the eastern Lake Agassiz-Ojibway basin, *Quat. Sci. Rev.*, 223, 105942,
489 <https://doi.org/10.1016/j.quascirev.2019.105942>, 2019.

490 Godbout, P. M., Roy, M., and Veillette, J. J.: A detailed lake-level reconstruction shows evidence for two abrupt lake
491 drawdowns in the late-stage history of the eastern Lake Agassiz-Ojibway basin, *Quat. Sci. Rev.*, 238, 106327,
492 <https://doi.org/10.1016/j.quascirev.2020.106327>, 2020.

493 Griffiths, M., Drysdale, R., Gagan, M., Frisia, S., Zhao, J., Ayliffe, L., Hantoro, W., Hellstrom, J., Fischer, M., and
494 Feng, Y.: Evidence for Holocene changes in Australian-Indonesian monsoon rainfall from stalagmite trace element
495 and stable isotope ratios, *Earth Planet. Sci. Lett.*, 292, 27–38, <https://doi.org/10.1016/j.epsl.2010.01.002>, 2010.

496 He, C., Liu, Z., Otto-Bliesner, B. L., Brady, E. C., Zhu, C., Tomas, R., and Bao, Y.: Hydroclimate footprint of pan-
497 Asian monsoon water isotope during the last deglaciation, *Sci. Adv.*, 7, eabe2611,
498 <https://doi.org/10.1126/sciadv.abe2611>, 2021.

499 Hersbach, H., Bell, B., Berrisford, P., Hirahara, S., Horányi, A., and Muñoz-Sabater, J.: The ERA5 global reanalysis,
500 *Q. J. R. Meteorol. Soc.*, 146, 1999–2049, <https://doi.org/10.1002/qj.3803>, 2020.

501 Hijma, M. P., and Cohen, K. M.: Timing and magnitude of the sea-level jump prelude the 8200 yr event, *Geology*,
502 38, 275–278, <https://doi.org/10.1130/G30439.1>, 2010.

503 Hughen, K. A., Overpeck, J. T., Peterson, L. C., and Trumbore, S.: Rapid climate changes in the tropical Atlantic
504 region during the last deglaciation, *Nature*, 380, 51–54, <https://doi.org/10.1038/380051a0>, 1996.

505 Jansson, K. N., and Kleman, J.: Early Holocene glacial lake meltwater injections into the Labrador Sea and Ungava
506 Bay, *Paleoceanography*, 19, PA1001, <https://doi.org/10.1029/2003PA000943>, 2004.

507 Jennings, A., Andrews, J., Pearce, C., Wilson, L., and Ólafsadóttir, S.: Detrital carbonate peaks on the Labrador shelf,
508 a 13–7 ka template for freshwater forcing from the Hudson Strait outlet of the Laurentide Ice Sheet into the subpolar
509 gyre, *Quat. Sci. Rev.*, 107, 62–80, <https://doi.org/10.1016/j.quascirev.2014.10.022>, 2015.

510 Johnson, K. R., Hu, C., Belshaw, N. S., and Henderson, G. M.: Seasonal trace-element and stable-isotope variations
511 in a Chinese speleothem: The potential for high-resolution paleomonsoon reconstruction, *Earth Planet. Sci. Lett.*, 244,
512 394–407, <https://doi.org/10.1016/j.epsl.2006.01.064>, 2006.

513 Kerwin, M. W.: A regional stratigraphic isochron (ca. 8000 ¹⁴C yr BP) from final deglaciation of Hudson Strait, *Quat*
514 *Res.*, 46, 89–98, <https://doi.org/10.1006/qres.1996.0049>, 1996.

515 Kleiven, H. K. F., Kissel, C., Laj, C., Ninnemann, U. S., Richter, T. O., and Cortijo, E.: Reduced North Atlantic deep
516 water coeval with the glacial Lake Agassiz freshwater outburst, *Science*, 319, 60–64,
517 <https://doi.org/10.1126/science.1148924>, 2008.

518 Kobashi, T., Menviel, L., Jeltsch-Thömmes, A., Vinther, B. M., Box, J. E., and Muscheler, R.: Volcanic influence on
519 centennial to millennial Holocene Greenland temperature change, *Sci. Rep.*, 7, 1–10, <https://doi.org/10.1038/s41598-017-01451-7>, 2017.

521 Kobashi, T., Severinghaus, J. P., Brook, E. J., Barnola, J.-M., and Grachev, A. M.: Precise timing and characterization
522 of abrupt climate change 8200 years ago from air trapped in polar ice, *Quat. Sci. Rev.*, 26, 1212–1222,
523 <https://doi.org/10.1016/j.quascirev.2007.01.009>, 2007.

524 Krklec, K., and Dominguez-Villar, D.: Quantification of the impact of moisture source regions on the oxygen isotope
525 composition of precipitation over Eagle Cave, central Spain, *Geochim. Cosmochim. Acta.*, 134, 39–54,
526 <https://doi.org/10.1016/j.gca.2014.03.011>, 2014.

527 Lajeunesse, P., and St-Onge, G.: The subglacial origin of the Lake Agassiz-Ojibway final outburst flood, *Nat. Geosci.*,
528 1, 184–188, <https://doi.org/10.1038/ngeo130>, 2008.

529 Lawrence, T., Long, A. J., Gehrels, W. R., Jackson, L. P., and Smith, D. E.: Relative sea-level data from southwest
530 Scotland constrain meltwater-driven sea-level jumps prior to the 8.2 kyr BP event, *Quat. Sci. Rev.*, 151, 292–308,
531 <https://doi.org/10.1016/j.quascirev.2016.06.013>, 2016.

532 LeGrande, A. N., and Schmidt, G. A.: Ensemble, water isotope-enabled, coupled general circulation modeling insights
533 into the 8.2 ka event, *Paleoceanography*, 23, PA3207, <https://doi.org/10.1029/2008PA001610>, 2008.

534 Li, H., Cheng, H., and Wang, J.: Applications of laser induced breakdown spectroscopy to paleoclimate research:
535 reconstructing speleothem trace element records, *Quat Sci.*, 38, 1549–1551 (in Chinese), 2018.

536 Li, H., Sinha, A., Anquetil André, A., Spötl, C., Vonhof, H. B., Meunier, A., and Cheng, H.: A multimillennial climatic
537 context for the megafaunal extinctions in Madagascar and Mascarene Islands, *Sci. Adv.*, 6, eabb2459,
538 <https://doi.org/10.1126/sciadv.abb2459>, 2020.

539 Li, X., Cheng, H., Tan, L., Ban, F., Sinha, A., and Duan, W.: The East Asian summer monsoon variability over the
540 last 145 years inferred from the Shihua Cave record, North China, *Sci. Rep.*, 7, 7078, [https://doi.org/10.1038/s41598-](https://doi.org/10.1038/s41598-017-07251-3)
541 017-07251-3, 2017.

542 Li, Y., Rao, Z., Xu, Q., Zhang, S., Liu, X., Wang, Z., and Chen, F.: Inter-relationship and environmental significance
543 of stalagmite $\delta^{13}\text{C}$ and $\delta^{18}\text{O}$ records from Zhenzhu Cave, north China, over the last 130 ka, *Earth Planet. Sci. Lett.*,
544 536, 116149, <https://doi.org/10.1016/j.epsl.2020.116149>, 2020.

545 Liu, D., Wang, Y., Cheng, H., Edwards, R. L., and Kong, X.: Cyclic changes of Asian monsoon intensity during the
546 early mid-Holocene from annually-laminated stalagmites, central China, *Quat. Sci. Rev.*, 121, 1–10,
547 <https://doi.org/10.1016/j.quascirev.2015.05.003>, 2015.

548 Liu, Y., Henderson, G. M., Hu, C., Mason, A. J., Charnley, N., and Johnson, K. R.: Links between the East Asian
549 monsoon and north Atlantic climate during the 8,200 year event, *Nat. Geosci.*, 6, 117–120,
550 <https://doi.org/10.1038/ngeo1708>, 2013.

551 Liu, Z., Wen, X., Brady, E. C., Otto-Bliesner, B., Yu, G., Lu, H., and Yang, H.: Chinese cave records and the East
552 Asia summer monsoon, *Quat. Sci. Rev.*, 83, 115–128, <https://doi.org/10.1016/j.quascirev.2013.10.021>, 2014.

553 Lochte, A. A., Repschläger, J., Kienast, M., Garbe-Schönberg, D., Andersen, N., and Hamann, C.: Labrador Sea
554 freshening at 8.5 ka BP caused by Hudson Bay Ice Saddle collapse, *Nat. Commun.*, 10, 1–9,
555 <https://doi.org/10.1038/s41467-019-08408-6>, 2019.

556 Ma, Z., Cheng, H., Tan, M., Edwards, R. L., Li, H., and You, C.: Timing and structure of the Younger Dryas event in
557 northern China, *Quat. Sci. Rev.*, 41, 83–93, <https://doi.org/10.1016/j.quascirev.2012.03.006>, 2012.

558 Matero, I. S. O., Gregoire, L. J., Ivanovic, R. F., Tindall, J. C., and Haywood, A. M.: The 8.2 ka cooling event caused
559 by Laurentide ice saddle collapse, *Earth Planet. Sci. Lett.*, 473, 205–214, <https://doi.org/10.1016/j.epsl.2017.06.011>,
560 2017.

561 Matero, I. S., Gregoire, L. J., and Ivanovic, R. F.: Simulating the Early Holocene demise of the Laurentide Ice Sheet
562 with BISICLES (public trunk revision 3298), *Geosci. Model. Dev.*, 13, 4555–4577, [https://doi.org/10.5194/gmd-13-](https://doi.org/10.5194/gmd-13-4555-2020)
563 4555-2020, 2020.

564 McDermott, F.: Palaeo-climate reconstruction from stable isotope variations in speleothems: a review, *Quat. Sci. Rev.*,
565 23, 901–918, <https://doi.org/10.1016/j.quascirev.2003.06.021>, 2004.

566 Mjell, T. L., Ninnemann, U. S., Eldevik, T., and Kleiven, H. K. F.: Holocene multidecadal-to millennial-scale
567 variations in Iceland-Scotland overflow and their relationship to climate, *Paleoceanography*, 30, 558–569,
568 <https://doi.org/10.1002/2014PA002737>, 2015.

569 Morrill, C., Anderson, D. M., Bauer, B. A., Buckner, R., Gille, E. P., Gross, W. S., Hartman, M., and Shah, A.: Proxy
570 benchmarks for intercomparison of 8.2 ka simulations, *Clim. Past.*, 9, 423–432, <https://doi.org/10.5194/cp-9-423-2013>,
571 2013.

572 Morrill, C., Ward, E. M., Wagner, A. J., Otto-Bliesner, B. L., and Rosenbloom, N.: Large sensitivity to freshwater
573 forcing location in 8.2 ka simulations., *Paleoceanography*, 29, 930–945, <https://doi.org/10.1002/2014PA002669>, 2014.

574 Peros, M., Collins, S., G'Meiner, A. A., Reinhardt, E., and Pupo, F. M.: Multistage 8.2 kyr event revealed through
575 high-resolution XRF core scanning of Cuban sinkhole sediments, *Geophys. Res. Lett.*, 44, 7374–7381,
576 <https://doi.org/10.1002/2017GL074369>, 2017.

577 Polyak, V. J., Rasmussen, J. B., and Asmerom, Y.: Prolonged wet period in the southwestern United States through
578 the Younger Dryas, *Geology*, 32, 5–8, <https://doi.org/10.1130/G19957.1>, 2004.

579 Renold, M., Raible, C. C., Yoshimori, M., and Stocker, T. F.: Simulated resumption of the North Atlantic meridional
580 overturning circulation-slow basin-wide advection and abrupt local convection, *Quat. Sci. Rev.*, 29, 101–112,
581 <https://doi.org/10.1016/j.quascirev.2009.11.005>, 2010.

582 Rohling, E. J., and Pälike, H.: Centennial-scale climate cooling with a sudden cold event around 8,200 years ago,
583 *Nature*, 434, 975–979, <https://doi.org/10.1038/nature03421>, 2005.

584 Roy, M., Dell'Oste, F., Veillette, J. J., De Vernal, A., Hélié, J. F., and Parent, M.: Insights on the events surrounding
585 the final drainage of Lake Ojibway based on James Bay stratigraphic sequences, *Quat. Sci. Rev.*, 30, 682–692,
586 <https://doi.org/10.1016/j.quascirev.2010.12.008>, 2011.

587 **Scholz, D., and Hoffmann, D. L.: *StalAge-An algorithm designed for construction of speleothem age models. *Quat****
588 ***Geochronol.* 6, 369–382, <https://doi.org/10.1016/j.quageo.2011.02.002>, 2011.**

589 Sodemann, H., Schwierz, C., and Wernli, H.: Interannual variability of Greenland winter precipitation sources:
590 Lagrangian moisture diagnostic and North Atlantic Oscillation influence, *J. Geophys. Res. -Atmos.*, 113, D3107,
591 <https://doi.org/10.1029/2007JD008503>, 2008.

592 Spurk, M., Leuschner, H. H., Baillie, M. G., Briffa, K. R., and Friedrich, M.: Depositional frequency of German
593 subfossil oaks: climatically and non-climatically induced fluctuations in the Holocene, *Holocene*, 12, 707–715, 2002.

594 Stein, A. F., Draxler, R. R., Rolph, G. D., Stunder, B. J., Cohen, M. D., and Ngan, F.: NOAA's HYSPLIT atmospheric
595 transport and dispersion modeling system, *B. Am. Meteorol. Soc.*, 96, 2059–2077, <https://doi.org/10.1175/BAMS-D-14-00110.1>, 2015.

597 Steinhilber, F., Beer, J., and Fröhlich, C.: Total solar irradiance during the Holocene, *Geophys. Res. Lett.*, 36,
598 <https://doi.org/10.1029/2009GL040142>, 2009.

599 Stríkis, N. M., Cruz, F. W., Cheng, H., Karmann, I., Edwards, R. L., and Vuille, M.: Abrupt variations in South
600 American monsoon rainfall during the Holocene based on a speleothem record from central-eastern Brazil, *Geology*,
601 39, 1075–1078, <https://doi.org/10.1130/G32098.1>, 2011.

602 Tan, L., Li, Y., Wang, X., Cai, Y., Lin, F., Cheng, H., Ma, L., Sinha, A., and Edwards, R. L.: Holocene monsoon
603 change and abrupt events on the western Chinese Loess Plateau as revealed by accurately dated stalagmites, *Geophys.*
604 *Res. Lett.*, 47, e2020GL090273, <https://doi.org/10.1029/2020GL090273>, 2020.

605 Teller, J. T., Leverington, D. W., and Mann, J. D.: Freshwater outbursts to the oceans from glacial Lake Agassiz and
606 their role in climate change during the last deglaciation, *Quat. Sci. Rev.*, 21, 879–887, [https://doi.org/10.1016/S0277-
607 *3791\(01\)00145-7*, 2002.](https://doi.org/10.1016/S0277-3791(01)00145-7)

608 Thomas, E. R., Wolff, E. W., Mulvaney, R., Steffensen, J. P., Johnsen, S. J., and Arrowsmith, C.: The 8.2 ka event
609 from Greenland ice cores, *Quat. Sci. Rev.*, 26, 70–81, <https://doi.org/10.1016/j.quascirev.2006.07.017>, 2007.

610 Törnqvist, T. E., and Hijma, M. P.: Links between early Holocene ice-sheet decay, sea-level rise and abrupt climate
611 change, *Nat. Geosci.*, 5, 601–606, <https://doi.org/10.1038/ngeo1536>, 2012.

612 Voarintsoa, N. R. G., Matero, I. S., Railsback, L. B., Gregoire, L. J., Tindall, J., Sime, L., and Razanatseheno, M. O.
613 M.: Investigating the 8.2 ka event in northwestern Madagascar: Insight from data-model comparisons, *Quat. Sci. Rev.*,
614 204, 172–186, <https://doi.org/10.1016/j.quascirev.2018.11.030>, 2019.

615 Von Grafenstein, U., Erlernkeuser, H., and Trimborn, P.: Oxygen and carbon isotopes in modern fresh-water ostracod
616 valves: assessing vital offsets and autecological effects of interest for palaeoclimate studies, *Palaeogeogr.*
617 *Palaeoclimatol. Palaeoecol.*, 148, 133–152, [https://doi.org/10.1016/S0031-0182\(98\)00180-1](https://doi.org/10.1016/S0031-0182(98)00180-1), 1999.

618 Wagner, A. J., Morrill, C., Otto-Bliesner, B. L., Rosenbloom, N., and Watkins, K. R.: Model support for forcing of
619 the 8.2 ka event by meltwater from the Hudson Bay ice dome, *Clim. Dyn.*, 41, 2855–2873,
620 <https://doi.org/10.1007/s00382-013-1706-z>, 2013.

621 Wang, X., Auler, A. S., Edwards, R. L., Cheng, H., Cristalli, P. S., Smart, P. L., and Shen, C. C.: Wet periods in
622 northeastern Brazil over the past 210 kyr linked to distant climate anomalies, *Nature*, 432, 740–743,
623 <https://doi.org/10.1038/nature03067>, 2004.

624 Wanner, H., Solomina, O., Grosjean, M., Ritz, S. P., and Jetel, M.: Structure and origin of Holocene cold events, *Quat.*
625 *Sci. Rev.*, 30, 3109–3123, <https://doi.org/10.1016/j.quascirev.2011.07.010>, 2011.

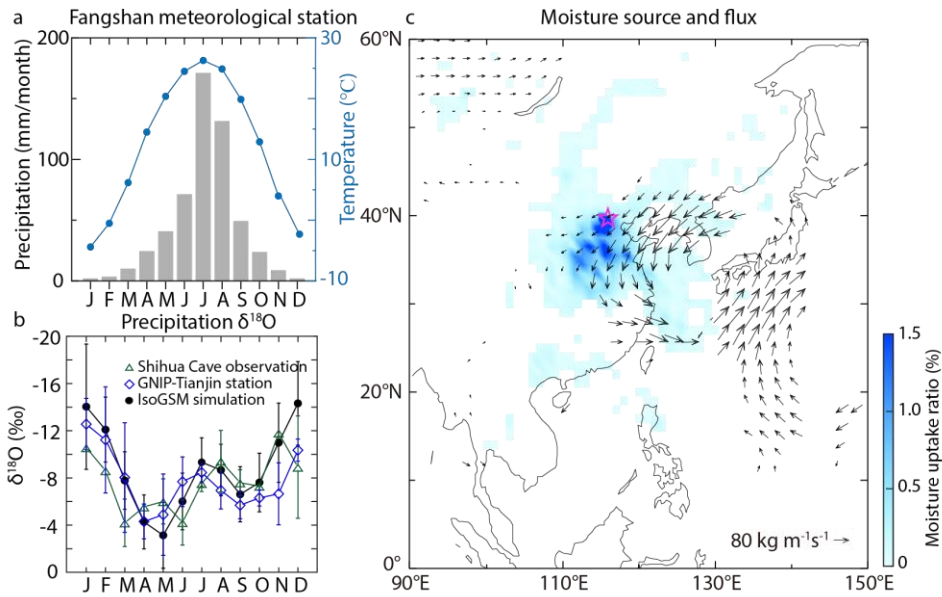
626 Wong, C. I., Banner, J. L., and Musgrove, M.: Holocene climate variability in Texas, USA: An integration of existing
627 paleoclimate data and modeling with a new, high-resolution speleothem record, *Quat. Sci. Rev.*, 127, 155–173,
628 <https://doi.org/10.1016/j.quascirev.2015.06.023>, 2015.

629 **Wood, C. T., Johnson, K. R., Lewis, L. E., Wright, K., Wang, J. K., and Borsato, A.: High-resolution, multiproxy**
630 **speleothem record of the 8.2 ka event from Mainland Southeast Asia. *Paleoceanogr Paleocl*, 38, e2023PA004675.**
631 **<https://doi.org/10.1029/2023PA004675>, 2023.**

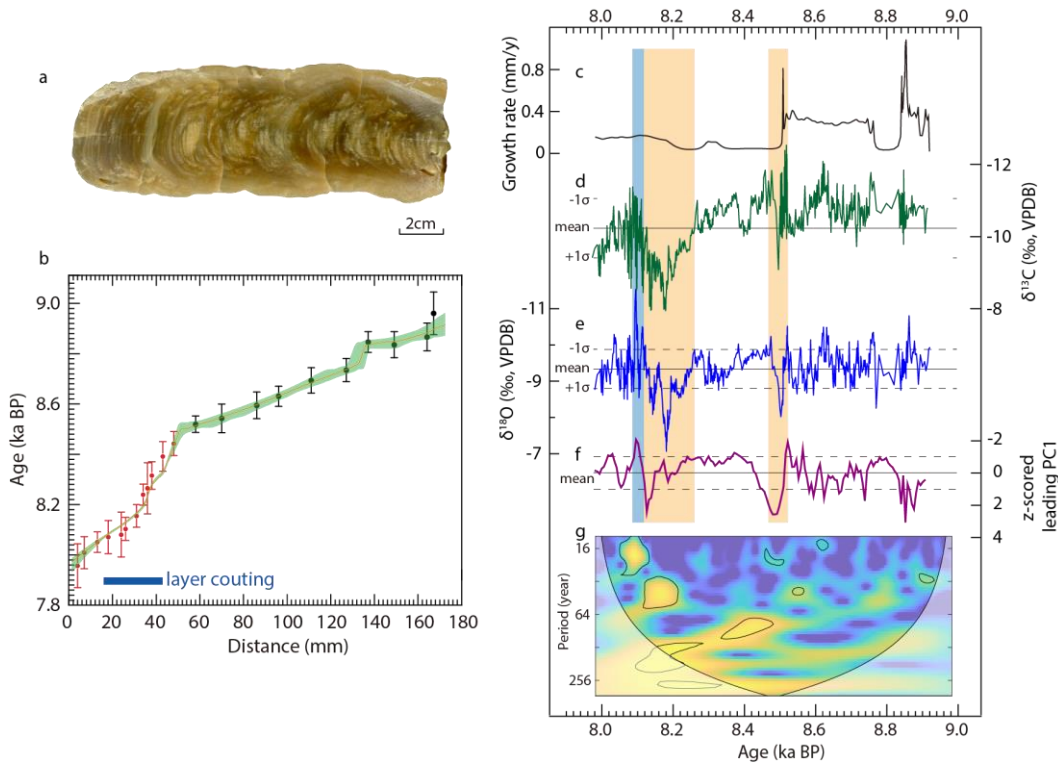
632 Yoshimura, K., Kanamitsu, M., Noone, D., and Oki, T.: Historical isotope simulation using reanalysis atmospheric
633 data, *J. Geophys. Res. -Atmos.*, 113, D19108, <https://doi.org/10.1029/2008JD010074>, 2008.

634 Zhang, H., Griffiths, M. L., Chiang, J. C., Kong, W., Wu, S., Atwood, A., and Xie, S.: East Asian hydroclimate
635 modulated by the position of the westerlies during Termination I, *Science*, 362, 580–583,
636 <https://doi.org/10.1126/science.aat9393>, 2018.

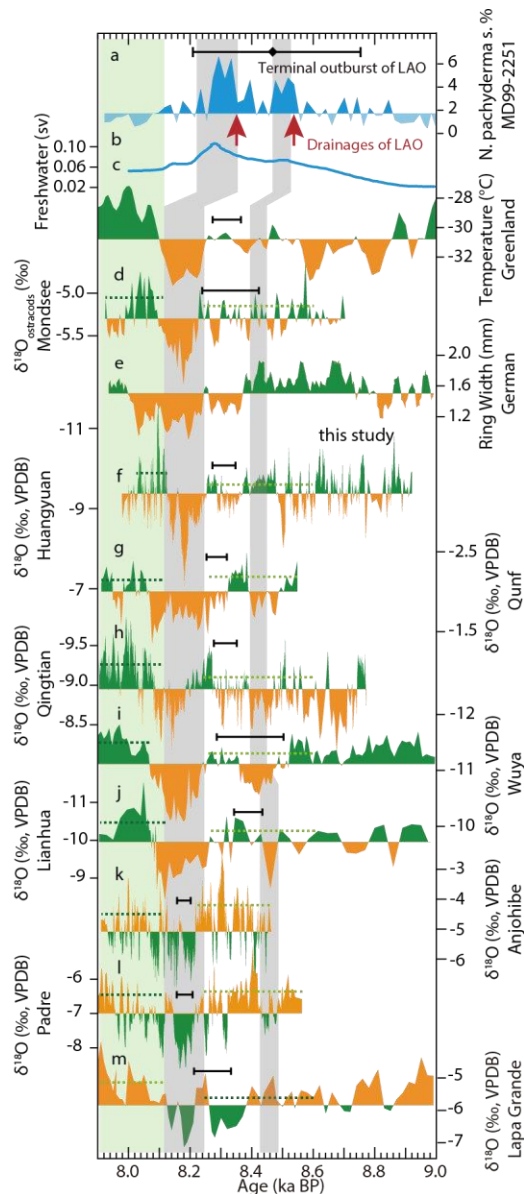
637 Zhao, J., Cheng, H., Cao, J., Sinha, A., Dong, X., Pan, L., Pérez-Mejías, C., Zhang, H., Li, H., Wang, J., Wang, K.,
638 Cui, J., and Yang, Y.: Orchestrated decline of Asian summer monsoon and Atlantic meridional overturning circulation
639 in global warming period, *The Innovat. Geosci.*, 1, 100011, <https://doi.org/10.59717/j.xinn-geo.2023.100011>, 2023.



640
 641 **Figure 1. Climatology and locations.** (a) Climographs of precipitation amount (gray bars) and temperature (blue dots
 642 connected with lines) at Fangshan Station (39°46'N, 116°28'E) near the study site, based on Chinese Meteorological
 643 Administration data (<http://www.cma.gov.cn/>). (b) Annual cycle comparison of $\delta^{18}\text{O}_p$ from observations of GNIP
 644 Tianjin station (<https://www.iaea.org/services/networks/gnip>) (1988–2002 CE with absent data covering 1993–2000
 645 CE, blue triangles), Shihua Cave (Duan et al., 2016) (2011–2014 CE, green diamonds), and IsoGSM-simulation data
 646 (Yoshimura et al., 2008) (1979–2017 CE, black dots) at the Huangyuan Cave. Error bars represent the 1 σ uncertainty
 647 of $\delta^{18}\text{O}_p$ values for each month. (c) Mean July-August (JA) moisture source region (blue shading) the Hybrid Single
 648 Particle Lagrangian Integrated Trajectory (HYSPLIT) model version 4.0 (Stein et al., 2015) based on the NOAA-
 649 NCEP/NCAR reanalysis global meteorological field data of 2010–2020 CE (Sodemann et al., 2008; Krklec and
 650 Dominguez-Villar, 2014) and water vapor flux (arrow) from the European Centre for Medium-Range Weather
 651 Forecasts Reanalysis fifth-generation dataset (ERA5) (Hersbach et al., 2020) between 1980 and 2015 CE.



652
 653 **Figure 2. Age model and proxy profiles of speleothem BH-2.** (a) Scanned image of speleothem BH-2. **The scale of**
 654 **sample is similar with the x-axis of the subpanel b.** (b) **Stalage-derived age model** (red, Scholz and Hoffmann, 2011)
 655 **with 95 % confidence interval** (light blue shading). Error bars on ^{230}Th dates represent 2σ analytical errors. **The red**
 656 **dates indicate the published results of Duan et al. (2023).** The horizontal blue bar marks the range with layer counting.
 657 (c) The inferred growth rate of the BH-2 based on the chronology in (b). (d) and (e) are $\delta^{18}\text{O}$ (dark blue) and $\delta^{13}\text{C}$
 658 (green) profiles, respectively. The mean (solid) and the $\pm 1\sigma$ values (dashed) for each entire record are indicated by the
 659 horizontal lines. (f) 30-year loess filtered z-scored leading PC1 record of trace element ratios of Ba/Ca, Mg/Ca, and
 660 Sr/Ca (see Figure S3). The mean value of the PC1 record is presented. (g) **Wavelet periodicity analysis result of $\delta^{18}\text{O}$.**
 661 **The 10% significance level against red noise is shown as a thick contour.** The vertical yellow bars in the right subpanel
 662 mark the anomalously positive episodes and the light blue bar indicates the subsequent $\delta^{18}\text{O}$ overshoot after the 8.2
 663 ka event.



664
665
666
667
668
669
670
671
672
673
674
675

Figure 3. Comparisons of the BH-2 $\delta^{18}\text{O}$ record with records from circum-North Atlantic, ASM domain and South America. (a) *N.pachyderma.abundance* record from MD03-2665, North Atlantic (Ellison et al., 2006). The black diamond and error bar on the top indicate the dating of terminal outburst of LAO (Barber et al., 1999). The red arrows point to the two-step drainages of LAO into the North Atlantic. (b) Modelled freshwater flux from Laurentide Ice Sheet in unit of Sverdrups (Sv) (Matero et al., 2020). (c) Reconstructed temperature in Greenland (Kobashi et al., 2017). (d) $\delta^{18}\text{O}_{\text{ostracods}}$ record from Modsee, Austria (Andersen et al., 2017). (e) Ring width of tree from Germany (Spurk et al., 2002). (f) The BH-2 $\delta^{18}\text{O}$ record from Huangyuan Cave, Beijing (this study). (g) High-resolution $\delta^{18}\text{O}$ record (Fleitmann et al., 2003) from Qunf Cave with more precise ages (Cheng et al., 2009) (h) $\delta^{18}\text{O}$ record from Qingtian Cave, China (Liu et al., 2015). (i) $\delta^{18}\text{O}$ record from Wuya Cave, Northwest China (Tan et al., 2020). (j) $\delta^{18}\text{O}$ record from Lianhua Cave, North China (Dong et al., 2018). (k) $\delta^{18}\text{O}$ record from Anjohibe Cave, Northwest Madagascar (Duan P et al., 2021). (l) High-resolution $\delta^{18}\text{O}$ record from Padre Cave, Brazil, on the Oxcal-derived

676 chronology based on the ^{230}Th dates of Cheng et al. (2009). **(m)** High-resolution $\delta^{18}\text{O}$ record from Lapa Grande Cave,
677 Brazil (Stríkis et al., 2011). The $\delta^{18}\text{O}$ scale of **k–m** is inverse to other speleothem records. The vertical gray shading
678 bars indicate the events centered at 8.5 and 8.2 ka BP and the green shading bar marks the post-8.2 ka event. The $\delta^{18}\text{O}$
679 value lower than the mean value of the entire records from the Northern Hemisphere, and Greenland reconstructed
680 temperature record higher than the mean value of the entire record is shaded in green. The $\delta^{18}\text{O}$ values higher than the
681 mean value of the entire records from the Southern Hemisphere are shaded in brown. The green horizontal dashed
682 lines in each record indicate the mean $\delta^{18}\text{O}$ values for the age range they cover before (8.60–8.22 ka BP) and after
683 (8.10–7.90 ka BP) the 8.2 ka event. The typical error of dating are shown as black bar in each curve.